Sea Surface Signature of Internal Tides

Noé Lahaye[1] [ID] **, Jonathan Gula[1]** [ID] **, and Guillaume Roullet[1]** [ID]

[1]Université de Bretagne Occidentale, CNRS, IRD, Ifremer, Laboratoire d'Océanographie Physique et Spatiale (LOPS), IUEM, Brest, France

Abstract The upper ocean is energetic at scales below the Rossby deformation radius owing to the existence of internal waves and submesoscale fronts and vortices. These contribute significantly to energy dissipation, tracer mixing, and exchanges between the ocean surface layer, the ocean interior, and the atmospheric boundary layer. Internal waves and submesoscale motions both undergo strong spatial and seasonal variations, driven by different mechanisms. Here, we investigate the sea surface signature of internal waves and its seasonality using linear wave theory and a high-resolution realistic simulation. In summer, internal waves are greatly amplified near the surface mostly due to a thin mixed layer bounded by a seasonal pycnocline. This surface amplification is well captured by linear theory, provided that the stratification at the base of the mixed layer is accurately represented. In winter, the superinertial motions are not fully explained by linear theory, reflecting impacts of the more energetic submesoscale motions.

1. Introduction

The ocean surface kinetic energy and sea surface height (SSH) variability are dominated by mesoscale eddies, at horizontal scales of the order of the internal Rossby deformation radius or larger. However, motions at scales below the internal Rossby deformation radius are also energetic and strongly impact the ocean circulation. These motions can be separated into contributions from internal waves and those due to submesoscale currents. Submesoscale currents are visible in the form of fronts, filaments, and vortices and are generated at the surface mostly by mixed layer instability and strain induced frontogenesis (McWilliams, 2016). Throughout this paper, "submesoscale motion" will refer to nonwave motion, with no implication for their balanced or unbalanced dynamics.

Submesoscale currents are instrumental in the ocean kinetic energy budget as they can trigger a direct turbulent cascade of energy from balanced motions down to dissipative scales (e.g., Ferrari & Wunsch, 2009; McWilliams, 2016). They also play an essential role in modifying momentum and heat exchange between the ocean and atmosphere (Renault et al., 2018; Su et al., 2018). Lastly, the strong vertical velocities associated with submesoscale fronts and filaments generate vertical fluxes of carbon and other biogeochemical tracers from the surface layer to the interior (Balwada et al., 2018) and drive the phytoplankton production (Lévy et al., 2018; Mahadevan, 2016). Likewise, internal waves can break near the surface, thus enhancing dissipation and mixing and playing an active role in the transfer of heat through the base of the mixed layer (Barton et al., 2001; Wain et al., 2015).

Submesoscale flows are difficult to measure as they are too fine for most satellite to resolve, and in particular the current generation of satellite altimeters ($\approx$100 km). In the near future, satellite measurements from the Surface Water and Ocean Topography mission (Fu & Ferrari, 2008) will provide a global coverage of SSH at unprecedented resolution (20 to 30 km). However, reconstructing the geostrophic surface velocity from SSH is a challenging task at these scales. In particular, the presence of unbalanced motions with similar spatial scales, such as internal waves and ageostrophic submesoscale currents, contaminates the estimates of the surface velocity. Our ability to compute the geostrophic surface velocity from SSH measurements will thus depend on our capacity to disentangle the signals associated with balanced and unbalanced motions. The low temporal sampling of satellites also prevents a direct filtering of high-frequency motions based on time averaging. More direct measurements of ocean surface velocity, as planned through projects under development such as the Sea surface Kinematics Multiscale mission (Ardhuin et al., 2018) and the Wind and Current Mission (Rodríguez et al., 2018), must also contend with this time aliasing. As a consequence, there has been a growing interest in understanding the surface signature of submesoscale processes and internal waves (e.g., Chelton et al., 2018; Savage et al., 2017; Torres et al., 2018). Their surface signature exhibits

strong seasonality and are usually out of phase (Callies et al., 2015; Qiu et al., 2018; Rocha et al., 2016). Indeed, submesoscale currents are highly energized by ubiquitous mixed layer instability in winter, while the internal waves can be surface amplified in summer. The latter is usually discussed following the work of D'Asaro (1978), who showed that the presence of a mixed layer and underlying density gap could support the existence of interfacial waves excited from the interior wave field, resulting in a drastic amplification of the surface kinetic energy near the surface. This associated amplification in summer was qualitatively reproduced by Rocha et al. (2016; supporting information), using stratification profiles from the World Ocean Atlas database (WOA13). With the exception of Rocha et al. (2016), not much effort has been dedicated to the validation of the idealized model of D'Asaro (1978) against actual observations or high-resolution modeling, while the mechanism described is regularly invoked (Callies & Ferrari, 2013; St. Laurent & Merrifield, 2017; Qiu et al., 2018; Torres et al., 2018).

In this paper, we concentrate on the dependence of the internal wave energetics with depth. More precisely, we compare the surface/interior amplitude ratio from linear theory and high-resolution realistic modeling over the north Mid-Atlantic Ridge. In this region, the internal tides significantly contribute to the surface kinetic energy and SSH fluctuations at scales below the Rossby deformation radius (Torres et al., 2018; Vic et al., 2018). Our results suggest that the surface amplification of internal waves is indeed well reproduced by a linear framework, although the details of the stratification in the mixed layer change substantially the shape of the surface/amplitude ratio as a function of horizontal wavenumber (and/or wave frequency). We conclude the study by providing global maps of the seasonal surface/interior amplitude ratio obtained by applying the linear theory to climatological stratification profiles.

2. Linear Amplification of Internal Waves

Linear internal waves in a horizontally uniform ocean with stratification $N(z)$ under the Boussinesq and hydrostatic approximations obey the following Sturm-Liouville equation (e.g., Gill, 1982; Wunsch, 2015)—formulated here in terms of the vertical velocity w:

$$\frac{\mathrm{d}^2 w}{\mathrm{d}z^2} + \kappa^2 \frac{N(z)^2}{\omega^2 - f^2} w = 0, \tag{1}$$

with Dirichlet boundary condition at $z = 0, -H$. Using the rigid-lid assumption does not prevent one from diagnosing the SSH η using the dynamical condition $p = \rho_0 g \eta$ at $z = 0$, where ρ_0 is the mean density and g the gravitational acceleration. The eigenvalue κ is the modulus of the horizontal wavenumber, ω the internal wave frequency, and f the Coriolis parameter. For the rest of the discussion, we introduce the variable $c = \sqrt{\omega^2 - f^2}/\kappa$. Under the hydrostatic approximation, the linear problem (1) thus depends on c alone instead of both κ and ω independently.

The standard WKBJ (Wentzel-Kramers-Brillouin-Jeffreys) solution to this equation is obtained by assuming that typical variations of $N(z)$ are small and/or have larger length scale than the waves (e.g., Gerkema & Zimmerman, 2008; Gill, 1982). For a vertical mode of index m, it is given by

$$w_m(z) = \frac{1}{\sqrt{N}} \sin\left(c_m^{-1} \int_{-H}^{z} N(z') \mathrm{d}z' \right), \tag{2}$$

up to an constant factor, and is associated with the eigenvalue:

$$c_m = \frac{\langle N \rangle H}{m\pi}, \tag{3}$$

where $\langle N \rangle$ is the depth-averaged Brunt-Väisälä frequency. Note that c_m is $R_m f$, where R_m is the internal Rossby radius associated with the mth eigenmode. Solutions to equation (1) describe the vertical structure of w-like fields and are linked to pressure-like fields (such as u and v) through the relation $\omega p/\rho_0 = ic^2 \mathrm{d}w/\mathrm{d}z$ (e.g., Wunsch, 2015). Horizontal velocities and, therefore, horizontal kinetic energy (HKE) are then obtained using the polarization relations (e.g., Gill, 1982). The WKBJ solution to these fields is similar to equation (2) with $\sin \to \cos$ and multiplied by $N(z)$.

2.1. Analytical Solution for an Idealized Stratification

A canonical model describing the solution to equation (1) and the sea surface signature of internal waves in the presence of a mixed layer was introduced by D'Asaro (1978), who assumed a mixed layer (with $N = 0$) capped by a buoyancy step Δb over a uniformly stratified interior ocean ($N = N_{\text{int}}$). Applying a matching condition at the interface between the mixed layer and the interior ocean (e.g., supporting information; Gerkema & Zimmerman, 2008, p. 86), and further assuming a continuous spectrum of internal waves coming from below (i.e., neglecting the finite depth of the ocean) and a very thin mixed layer $H_{\text{ml}} \ll \lambda_{\text{IW}}$ (where λ_{IW} is the vertical wavelength of the wave), he showed that the surface-to-interior HKE ratio for internal waves is

$$R(c) = \left[\frac{N_{\text{int}}^2 H_{\text{ml}}^2}{c^2} + \left(1 - \frac{\Delta b H_{\text{ml}}}{c^2} \right)^2 \right]^{-1}. \tag{4}$$

This expression describes the main linear mechanism that drives the sea surface amplitude of internal waves. In the absence of a density gap at the base of the mixed layer, $\Delta b = 0 \Rightarrow R(c) < 1$. Thus, the mixed layer acts as a low-pass filter in terms of the horizontal wavenumber ($\kappa \propto^{-1}$) with a κ^{-2} attenuation. However, for $\Delta b \neq 0$, interfacial waves can be excited when the term in parentheses approaches 0, that is, when $\Delta b \rightarrow c^2/H_{\text{ml}}$. The remaining term $N_{\text{int}}^2 H_{\text{ml}}^2 c^2$ is approximately $(H_{\text{ml}}/\lambda_{\text{IW}})^2 \ll 1$. This leads to a strong amplification of the wave signature for $c \approx \sqrt{\Delta b H_{\text{ml}}}$, and a strong attenuation ($\propto c^4$, i.e., κ^{-4}) at higher wavenumber.

2.2. Extension to a Realistic Stratification

While providing a qualitative explanation for the amplification, the simplified model of D'Asaro (1978) has several limitations. The stratification is assumed piecewise constant and therefore variations of the wave amplitude associated with the stratification (partly captured by the WKBJ solution; see equation (2) and below) are not taken into account. More important, the density step at the base of the mixed layer takes place over an infinitely thin layer. While one can have the intuition that low vertical wavenumber waves should not be affected, it should not be so for higher wavenumber waves, and thereby, the κ^{-4} fall-off could be dubious. Finally, the quantity used in the definition of $R(c)$—namely, the vertically integrated kinetic energy in the spectral domain—is not available in a realistic setup, because of the nonconstant bottom depth.

To alleviate these limitations, we generalize the previous solution by numerically solving equation (1) for (1) a fully realistic stratification profile and (2) a modified stratification using the realistic stratification profile below the mixed layer and $N = 0$ in the mixed layer. Furthermore, we also seek a third solution using the modified stratification and a WKBJ approximation in the ocean interior. This solution is obtained by numerically solving the transcendental equation that stems from matching the solutions in the interior (equation (2)) and in the mixed layer at the interface (Gerkema & Zimmerman, 2008). It provides an intermediate, semianalytical solution that partially captures the effects of nonuniform Brunt-Väisälä frequency, thus extending the solution introduced by D'Asaro (1978).

The surface-to-interior amplitude ratio is estimated based on an approximate amplitude for internal waves, scaled like the HKE:

$$A^2(\omega, c, z) = K_H + \frac{N^2(z)}{2\omega^2} \frac{\omega^2 + f^2}{\omega^2 - f^2} K_V, \quad R = \frac{A^2(z_{\text{surf}})}{A^2(z_{\text{int}})}, \tag{5}$$

where K_H and K_V are the horizontal and vertical kinetic energy spectral densities, respectively. The oscillating vertical structure of K_H and K_V (reflecting the modal structure of the p-like and w-like solutions) approximately compensate each other in the quantity A^2, according to the WKBJ theory (see also supporting information), and A is approximately proportional to $\sqrt{N(z)}$. This "WKBJ amplitude" provides a way to estimate the interior wave amplitude freed from the impact of variable stratification and depth and allows us to make quantitative comparisons between numerical simulations and the linear theory, as shown below. The reference level at which A is evaluated in the interior is $z_{\text{int}} = 500$ m, which is deep enough to avoid errors due to large variations of $N(z)$ and associated breakdown of WKBJ approximation. The surface value is computed at $z_{\text{surf}} = 0$, where K_V vanishes. The amplitude A, and thereby the ratio R, can be similarly expressed in the real horizontal space through Parseval's theorem (this does not hold for the frequency/time dimension).

We use typical summer and winter stratification profiles from the realistic simulation over the northern Mid-Atlantic ridge described below (section 3.1). They are horizontally and time averaged over the
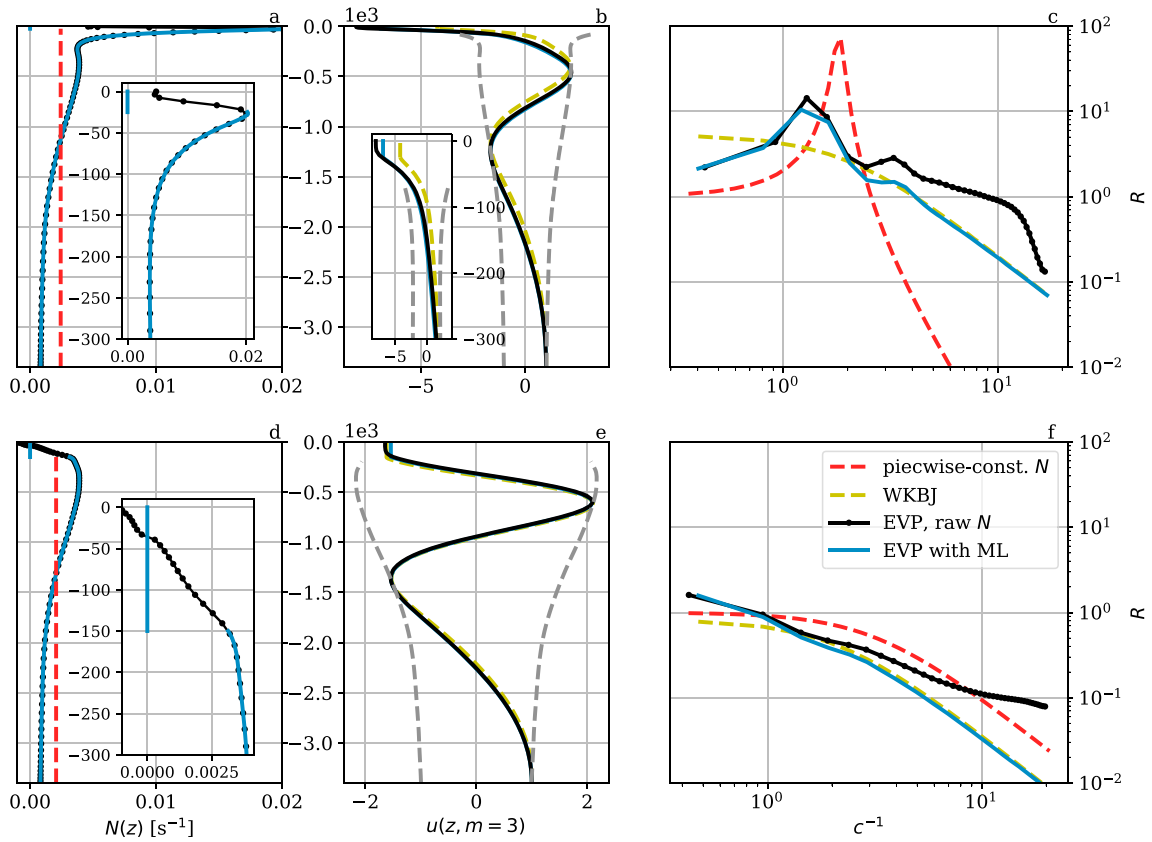
Figure 1. Summer (a–c) and winter (d–f) $N(z)$ profiles (a, d: averaged from the simulation), mode 3 vertical structure (b, e: normalized such that $u_m(-H) = 1$), and surface/interior ratio R as a function of c^{-1} (c, f), with c^{-1} corresponding to modes 1 to 40. Black: unmodified stratification. Blue: modified stratification (with $N = 0$ in the mixed layer). Green, dashed: WKBJ solution using the modified stratification. Red, dashed: piecewise-constant stratification, following D'Asaro (1978). For the latter, the value of Δb in summer is estimated as $\int_{-2H_{ml}}^{0} N^2(z)\mathrm{d}z$ (to integrate the entire peak), which gives $\Delta b = 0.012$ m/s^2. Gray dashed lines are the modal WKBJ-estimated amplitude $A_m(z)$, evaluated only below the pycnocline where $N(z) > 0$ and has moderate variations. WKBJ = Wentzel-Kramers-Brillouin-Jeffreys; EVP: Eigen Value Problem.

simulation domain for each season. The mean mixed layer depth is about 25 m in summer and 150 m in winter (Figure 1, left panels). The mean surface value of N^2 is negative in winter. The modal structure of the solutions and the surface-to-interior amplitude ratio $R(c^{-1})$ for each season are presented in Figure 1. We should stress here that c^{-1} can be read as a wavenumber at fixed frequency (this also holds for Figure 4). The modal structure (only mode 3 is shown) clearly exhibits a surface intensification in summer. The ratio $R(c)$ is plotted for all vertical mode numbers m up to 40, unless for D'Asaro's (1978) solution where the modal structure of the solution is neglected (and c is continuous). The surface amplification is qualitatively reproduced by the idealized model of D'Asaro (1978) as far as the presence of a peak is concerned. In winter, the $c^2 \propto \kappa^{-2}$ falloff is present in every solution. However, the magnitude and position of the peak and subsequent falloff in summer are overestimated with the analytical solution, while its spectral width, as well as the amplitude for lower modes, is underestimated. Both are due to a finite-width and finite-amplitude peak in the Brunt-Väisälä profile. On the other hand, the WKBJ solution fails in reproducing the amplification peak, probably because the variations of $N(z)$ below the seasonal pycnocline are too large and the resulting amplification is missing.

2.3. Horizontal Inhomogeneities

In a realistic context, the stratification is not horizontally homogeneous but is strongly altered by the mesoscale and submesoscale activity, especially near the surface and in winter. To get some insight into the impact of these horizontal inhomogeneities on the surface/interior ratio, we compute the solution of the linear eigenproblem 1 at a subsample of horizontal points in the domain considered, using a smoothed stratification (low-pass-filtered at 30 hr) from the realistic simulation. The result consists of maps of $R(c_m)$, where c_m varies in the domain because of variations of depth and stratification, and is shown in Figure 2 for
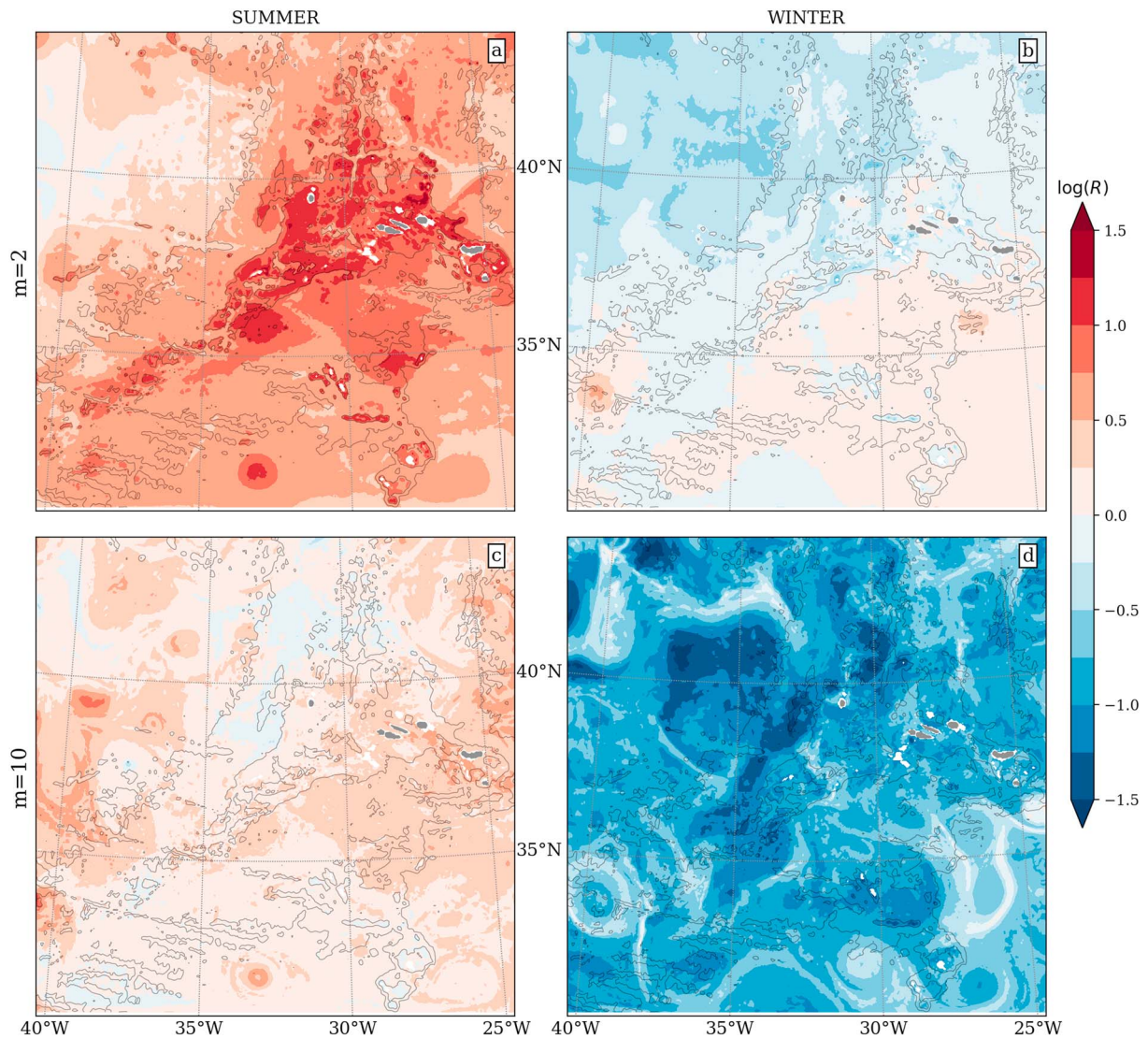
Figure 2. Surface/interior modal amplitude ratio R (logarithmic scale) computed using the stratification from the numerical simulation in summer (a, c) and winter (b, d), for the second (a, b) and tenth (c, d) baroclinic modes. Interior amplitude is taken at $z = -500$ m. Black lines are 2,000- and 3,500-m isobaths. The Mid-Atlantic Ridge crosses the domain on the southwest-northeast axis. Azores Islands (gray patches) are visible in the middle right region of the domain, around 38°N, 28°W.

modes 2 and 10. Changes in H or $\langle N \rangle$ are associated with a modification of c_m (following the approximate solution in equation (3)) virtually resulting in a shift of the mode along the curve $R(c)$ in Figure 1 (right panels), and thereby a change in the modal surface/interior amplitude ratio.

Indeed, the lowest vertical mode is dominated by the variations of the bottom depth H in summer (with maximum amplification over the ridge), and large-scale variations of the stratification in winter (slight amplification in the southeast sector, attenuation in the northwest). Mesoscale-induced horizontal variations of the stratification have no significant impact on the lowest modes, with the exception of the signature of an intense cyclone near the bottom of the domain (around 32°N, 33.5°W) in summer. Vortices and associated filaments are clearly distinguishable in the surface amplification patterns for the higher modes in winter (Figure 2d), with variations of $R(c_m)$ of about an order of magnitude.

3. Results From High-Resolution Realistic Modeling
3.1. Description of the Simulations
We use the Coastal and Regional Ocean COmmunity model (CROCO), which is based on the Regional Oceanic Modeling System (Shchepetkin & McWilliams, 2005), to simulate the flow in a domain spanning
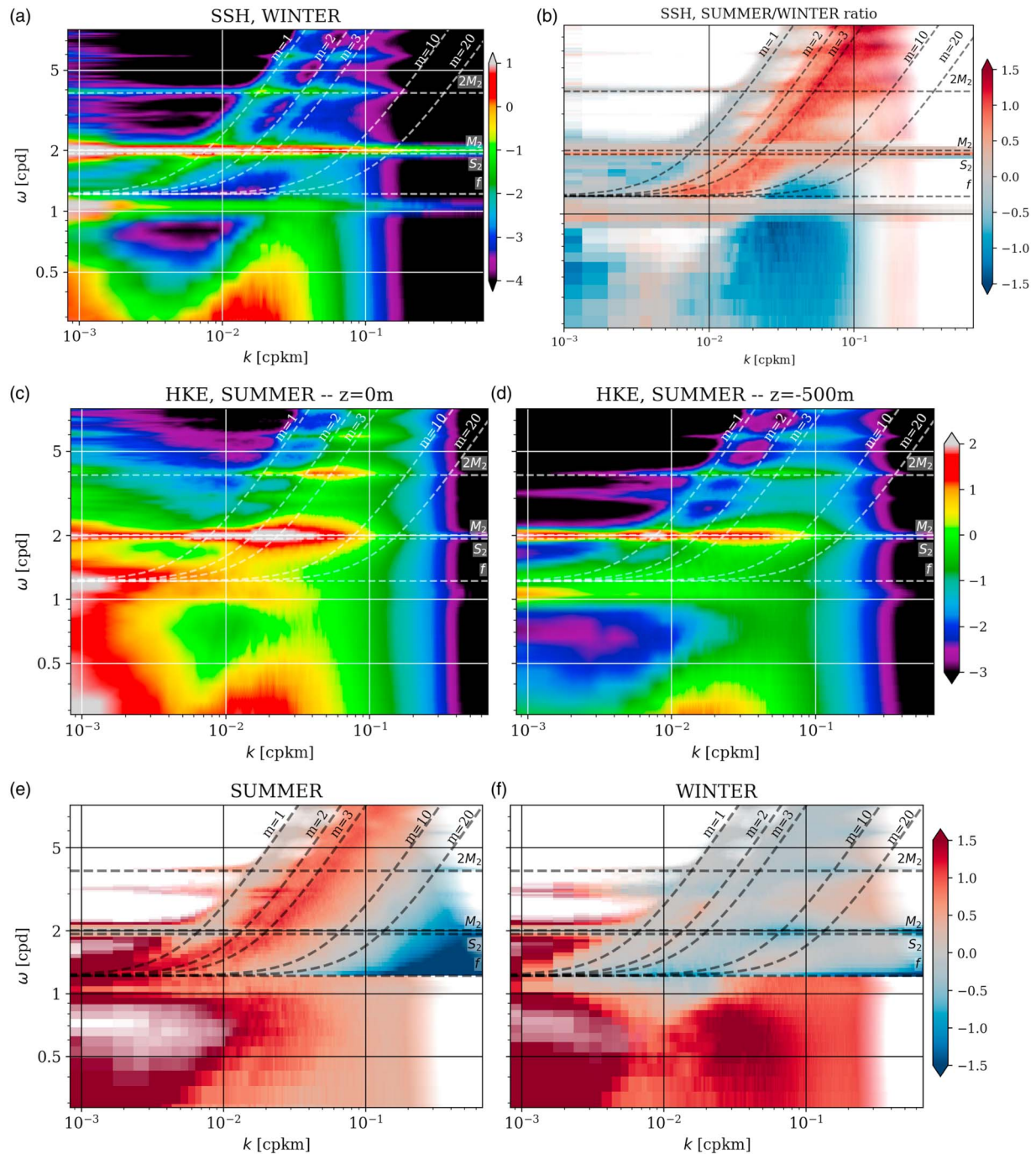
Figure 3. Power spectral density in the (k, ω) space (all plots are in log scale). Upper row: sea surface height (SSH) variance in winter (a) and summer/winter ratio (b). Middle row: summer horizontal kinetic energy (HKE) at the surface (c) and at depth ($z = -500$ m, d). Lower row: surface/interior amplitude ratio $R(k, \omega)$ in summer (e) and in winter (f). Ratios are displayed only where the corresponding spectral density is large enough, with colors fading to white in the range $(10^{-3}, 10^{-2})$ for A^2 and $(10^{-4}, 10^{-2.5})$ for the SSH.

$1,500 \times 1,500$ km around the Azores, with a horizontal resolution d$x = 750$ m and 80 vertical σ levels. The model integrates the Boussinesq hydrostatic primitive equations. The presence of the northern Mid-Atlantic Ridge is associated with intense internal tide activity (Vic et al., 2018). Typical ocean depth ranges between 1,000 m over the ridge and 5,000 m over the abyssal plain, with shallower regions around the Azores Islands. The simulation is a nest of a larger simulation that originates from a North-Atlantic run (more details are available in Vic et al., 2018). Tidal forcing interpolated from TPXO7.2 is added to the mesoscale forcing at

the boundaries, using the eight most important components. Tidal potential taken from GOT99.2b, as well as self-attraction and loading, is included throughout the domain. We compute the seasonal means in our domain by applying a low-pass time filter and spatial subsampling. We focus on 2-week periods representative of winter (15 February to 1 March) and summer (15 August to 1 September of the next year), out of a more-than-1-year run starting in July.

3.2. Motion Scales and Energy

The energetics of the different types of motion can be discussed based on power density spectra in the frequency-wavenumber domain (Figure 3, upper rows). In the upper part of the spectrum, the signature of internal tides is characterized by horizontal lines of high-energy density patches at the semidiurnal frequencies M_2, S_2 and their harmonics (M_4, etc.). The horizontal (k-wise) localization of these patches is representative of the modal structure of the waves and matches roughly the approximate dispersion relation derived from the mean depth of fluid and the mean value of N^2 (white oblique curves in the diagram). In between these tidal peaks, the energy is associated with an internal wave continuum, which is partially resolved within the simulation (Vic et al., 2018). The latter is probably too weak in the simulation, which lacks near-inertial waves due to daily winds forcings. The near-inertial peak is visible at the largest scales on the HKE, as well as its harmonics ($M_2 + f$, etc.) in the wave continuum band. At lower frequencies, a broad energetic patch roughly following a nondispersive line $\omega - v_\varphi k = 0$ (where v_φ is the phase speed of mesoscale eddies; Torres et al., 2018) is associated with the mesoscale ($50 < \lambda < 500$ km) and submesoscale ($1.5 < \lambda < 50$ km) dynamics. An overlap in space and time scales between (nonwave) submesoscale dynamics and internal waves is visible at scales between 5 and 50 km for superinertial frequencies up to $\omega = 2M_2$ in winter. In the same scale range, SSH is dominated by superinertial motions (i.e., roughly internal tides), in agreement with recent reports from a global MITgcm simulation (Torres et al., 2018). However, the sea surface kinetic energy is slightly dominated by subinertial motions.

Taking the ratio of the spectral density in summer over the one in winter clearly exhibits the different behavior between the internal waves and the submesoscale currents. The internal waves are more energetic in summer, especially for the vertical modes higher than the first baroclinic mode—the latter being roughly as intense in both season. On the contrary, the submesoscale motions are more energetic in winter (blue patch in Figure 3b).

Very little seasonal variation is visible in the near-inertial to diurnal frequency band, likely because of the dominance of the diurnal cycle and because diurnal internal tide cannot propagate at this latitude. No clear seasonal variation is observed at the semidiurnal (M_2, S_2) frequencies either. This is probably due to the dominance of the barotropic tide on the SSH variance at this frequency, even at scales smaller than the barotropic deformation radius. Indeed, the barotropic tide is modified by the topography (a process usually—but not necessarily—associated with the conversion to baroclinic tide), resulting in a broadening of the SSH variance toward high wavenumbers.

3.3. Sea Surface Amplification of Internal Tides and Seasonal Variations

We now focus on the surface amplification of internal waves by looking at the surface/interior ratio as discussed in the previous section 2.2. The lower row in Figure 3 shows the ratio $R(k, \omega)$ from equation (5) in summer and winter. At subinertial frequencies, the ratio is computed using the HKE only (as A is a quantity relevant for internal waves only). Qualitatively, these show good agreement with the theoretical expectations. The summer/winter ratio (upper right panel) exhibits a net amplification of $\mathcal{O}(10)$ magnitude along the dispersion curve corresponding to modes 2 to 4, at superinertial frequencies. The first baroclinic mode is very weakly amplified, and modes higher than 4 are damped for both seasons. The spectral amplitude ratio exhibits less variations in winter, but we observe a weak attenuation at the tidal frequencies and harmonics for every wavenumbers, and a weak amplification in between the tidal peaks. The presence of energetic submesoscale motions at the surface increases Doppler shift of waves and nonlinear interactions, which contributes to spreading energy from the tidal peaks to the background continuum.

A comparison between the results from the realistic simulations and theory for the ratio $R(c)$ is given for all $\omega > f$ in Figure 4. In summer, the agreement between the (black) curves at different frequencies is striking over the entire range of c^{-1} above the equivalent mode number 1. In addition, the agreement with the linear calculation using the realistic stratification is remarkably good, which altogether supports the fact that the surface/interior wave amplitude ratio is mainly driven by linear effects, and thus well described by equation (1). The high wavenumber (high c^{-1}) attenuation follows a c^2 power law, thus explained by a
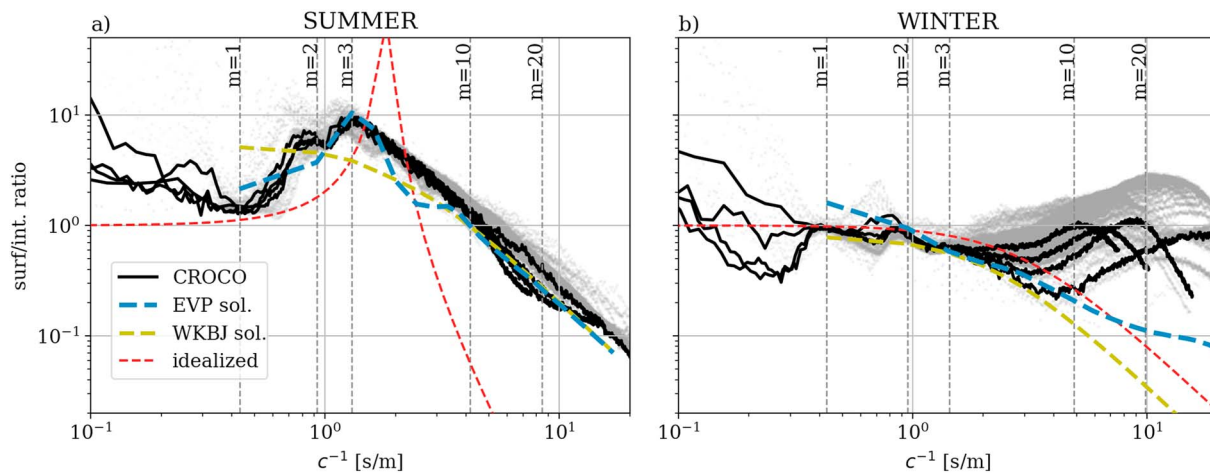
Figure 4. Surface/interior ($z = -500$ m) amplitude ratio versus c^{-1} in summer (a) and winter (b). Results from the realistic simulation are plotted in gray dots (with opacity proportional to the energy spectral density at 500 m, as in Figure 3, lower panels). Black curves are at tidal frequency M_2 and the first three harmonics. Blue, green, and red curves are the results from linear theory using averaged stratification with an imposed mixed layer—see Figure 1, except in winter for the numerical solution (the blue curve in the right panel corresponds to the black one in Figure 1f). CROCO = Coastal and Regional Ocean COmmunity model.

density step of finite width at the base of the mixed layer. As mentioned in section 2, the analytical solution using a constant N (red dashed line) uses severe assumptions and does not match the realistic model as well.

The agreement between the linear theory and simulation outputs is better if a well-mixed surface layer is imposed in the stratification profile used for the former (i.e., $N = 0$ at the surface—blue curve in Figure 1, left panels), in summer. Indeed, the averaged stratification profile (black curves in the same figure) exhibits slightly positive values near the surface because of the formation of a diurnal warm layer taking over the time-mean value (Bogdanoff, 2017), resulting in a power law slope shallower than -1 (Figure 1c), which is not what we observe in our numerical simulation. This is, in a way, a limitation of the validity of equation (1), which assumes a steady stratification.

In winter, the different curves coalesce over a smaller range of wavenumbers. The surface/interior ratio meets a minimal value followed by an increase until a cutoff wavenumber is reached (rapid decrease near the end of the curve). Below the value c^{-1} associated with this local minimum of R, the surface/interior ratio is well reproduced by the linear theory. The noncoalescing curve at larger c^{-1} means that the corresponding processes cannot be described by equation (1), since c is the only parameter. A plausible cause is the contamination by submesoscale motions in the corresponding region of the frequency/wavenumber spectra, consistent with the out-of-phase seasonality of mixed layer submesoscale motions and wave activity in the upper ocean. Indeed, the value k_c of minimum R increases with ω, which is in agreement with the nondispersive line followed by submesoscale motions in the frequency-wavenumber domain. In this context, this would be the manifestation of the transition scale being dependent of the frequency. Other possible explanations are the impact of horizontal inhomogeneities on the internal wave dynamics (equation (1) and thus $R(c)$ assumes an horizontally homogeneous environment), as discussed in section 2.3 and illustrated in Figure 2, and effects of restratification by the submesoscale turbulence (Boccaletti et al., 2007) and/or nonlinearities.

4. Discussion

As a result of the summer surface amplification of the internal tides, the high-frequency ($\omega > f$) mean surface HKE in our regional simulation is roughly 2.5 times larger in summer than in winter. However, the amplitude of SSH fluctuations exhibits less seasonal variations. Estimating the SSH associated with the internal tide by subtracting the barotropic signal estimated from TPXO7.2, we obtain that the high-frequency internal tide root-mean-square of SSH is about 5.2% of the barotropic signal in winter and 5.6% in summer. While we cannot exclude an imperfect internal tide signal extraction or the influence of unbalanced submesoscale motions, this result is consistent with the fact that internal tide signature on the SSH is largely dominated by the first baroclinic mode, which is not surface intensified. Henceforth, in the context of
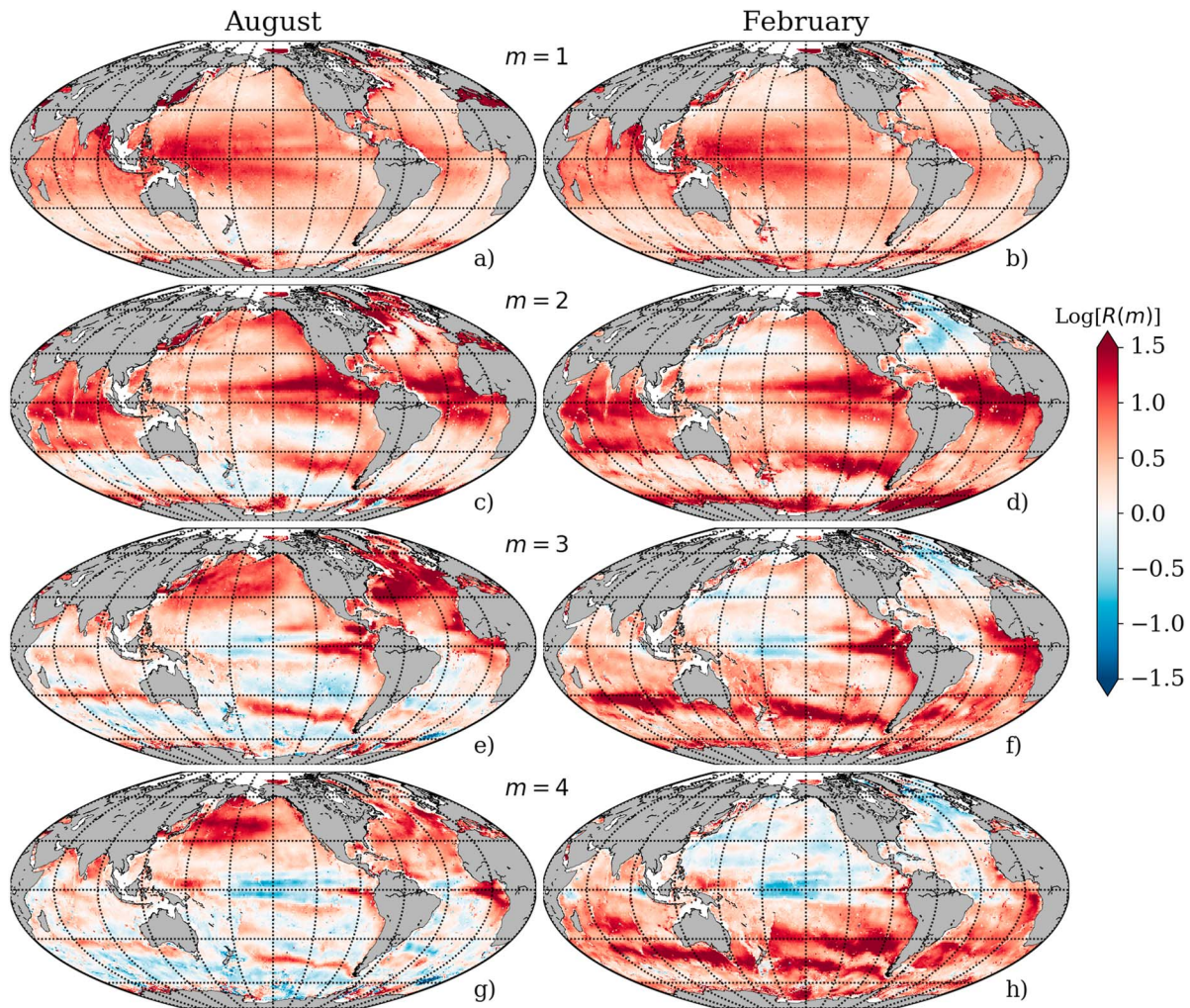
Figure 5. Global maps of modal surface/interior HKE ratio computed from monthly climatology in August (a, c, e, and g) and February (b, d, f, and h) for vertical modes 1 (a, b) to 4 (g, h).

(future) satellite measurements, the seasonal surface amplification of internal tides is directly visible in the velocity field but not in the SSH—unless smaller scales associated with the second or higher vertical modes are specifically targeted.

To provide some insight into the global implication of the amplification mechanism, we computed the amplification ratio for the world ocean using stratification from a monthly climatology (ISAS, see Gaillard, 2015; Gaillard et al., 2016) in February and August. Results for vertical modes 1 to 4 are shown in Figure 5. The properties of the amplification depicted previously are mostly recovered, with strong amplification for modes 3 in the summer hemisphere (a zoom over our study region is provided in supporting information Figure S1, for comparison with Figure 2). In addition, the signature of large-scale ocean dynamical features such as the Antarctic Circumpolar Current, the major western boundary currents (Gulf Stream and Kuroshio) as well as the thermocline structure in the equatorial band are clearly discernible. From the polarization relations and the dynamical condition at the sea surface ($p = \rho_0 g \eta$), the expression for the SSH amplitude reads:

$$|\eta| = \frac{c}{g} \sqrt{\frac{\omega^2 - f^2}{\omega^2 + f^2} \frac{R(c)}{2}} A(z_{\text{ref}}). \tag{6}$$

Combining the map in Figure 5 with the above expression and internal wave energy at the reference level (or, upon minor reformulation, of vertically integrated energy density or energy flux) results in SSH signature map on a global scale. Figure 5 also suggests that, in addition to the spatial inhomogeneities in the energy

density distribution that results from their generation and dissipation, the SSH signature of internal waves is modulated by the amplification mechanism associated with the stratification.

5. Conclusion

A better understanding of the surface signature of internal waves and the near-surface ocean dynamics is still needed, for example, in the context of satellite measurement of submesoscale dynamics. Recent studies have reported the surface amplification of the internal mode 3 in summer (Rocha et al., 2016; Torres et al., 2018) and noticed its importance in the seasonal variation of sea surface submesoscale activity. In this paper, we tested D'Asaro's (1978) proposed mechanism using results from high-resolution realistic simulations and showed that the linear dynamics of internal waves captures the essential properties of this amplification. In particular, we found that modes 2–4 are greatly amplified in summer, as previously reported, while internal modes are all attenuated in winter, due to a deeper mixed layer and the absence of a sharp density gap at its base.

Our results show that the details of the stratification profile are important for the amplification/attenuation role of the mixed layer. In particular, the sharpness of the density gradient changes the surface/interior kinetic energy ratio cutoff rate, which scales like $c^4 \propto \kappa^{-4}$ for an infinitely sharp step and $c^2 \propto \kappa^{-2}$ for a finite-width density gap, as well as the width and magnitude of the amplification peak. Sharp and stable mixed layers have been observed over limited periods in some regions of the ocean (e.g., St. Laurent & Merrifield, 2017), like during the formation of diurnal warm layer in the upper few meters, which has already been investigated in the context of internal wave dynamics (Bogdanoff, 2017, chapter 3). We also evidenced the potential impact of horizontal (sub)mesoscale inhomogeneities in the stratification near the surface on the internal wave activity, especially in winter. All together, these could result in strong horizontal and time dependence of the global sea surface signature of internal waves, which would need further investigation.

Finally, we should mention that nonlinear effects have not been discussed in this paper. We believe that the potential impact of this near-surface amplification on the generation of large-amplitude interfacial waves, such as solitons (Grisouard et al., 2011), or the breaking and associated mixing in the mixed layer (Wain et al., 2015), are worth being investigated in the near future.

References

Ardhuin, F., Aksenov, Y., Benetazzo, A., Bertino, L., Brandt, P., Caubet, E, et al. (2018). Measuring currents, ice drift, and waves from space: The Sea surface KInematics Multiscale monitoring (SKIM) concept. *Ocean Science*, *14*(3), 337–354. https://doi.org/10.5194/os-14-337-2018

Balwada, D., Smith, K. S., & Abernathey, R. (2018). Submesoscale vertical velocities enhance tracer subduction in an idealized Antarctic Circumpolar Current. *Geophysical Research Letters*, *45*, 9790–9802. https://doi.org/10.1029/2018GL079244

Barton, E. D, Inall, M. E, Sherwin, T. J, & Torres, R. (2001). Vertical structure, turbulent mixing and fluxes during Lagrangian observations of an upwelling filament system off Northwest Iberia. *Progress in Oceanography*, *51*(2), 249–267. https://doi.org/10.1016/S0079-6611(01)00069-6

Boccaletti, G., Ferrari, R., & Fox-Kemper, B. (2007). Mixed layer instabilities and restratification. *Journal of Physical Oceanography*, *37*(9), 2228–2250. https://doi.org/10.1175/JPO3101.1

Bogdanoff, A. S. (2017). Physics of diurnal warm layers: Turbulence, internal waves, and lateral mixing (PhD Thesis), MIT/WHOI Joint Program.

Callies, J., & Ferrari, R. (2013). Interpreting energy and tracer spectra of upper-ocean turbulence in the submesoscale range (1–200 km). *Journal of Physical Oceanography*, *43*(11), 2456–2474. https://doi.org/10.1175/JPO-D-13-063.1

Callies, J., Ferrari, R., Klymak, J., & Gula, J. (2015). Seasonality in submesoscale turbulence. *Nature Communications*, *6*, 6862. https://doi.org/10.1038/ncomms7862

Chelton, D. B., Schlax, M. G., Samelson, R. M., Farrar, J. T., Molemaker, M. J., McWilliams, J. C., & Gula, J. (2018). Prospects for future satellite estimation of small-scale variability of ocean surface velocity and vorticity. *Progress in Oceanography*. https://doi.org/10.1016/j.pocean.2018.10.012

D'Asaro, E. A. (1978). Mixed layer velocities induced by internal waves. *Journal of Geophysical Research*, *83*, 2437–2438.

Ferrari, R., & Wunsch, C. (2009). Ocean circulation kinetic energy: Reservoirs,sources, and sinks. *Annual Review of Fluid Mechanics*, *41*(1), 253–282. https://doi.org/10.1146/annurev.fluid.40.111406.102139

Fu, L.-L., & Ferrari, R. (2008). Observing oceanic submesoscale processes from space. *Eos, Transactions American Geophysical Union*, *89*(48), 488–488. https://doi.org/10.1029/2008EO480003

Gaillard, F. (2015). ISAS-13-CLIM temperature and salinity gridded climatology. SEANOE. https://doi.org/10.17882/45946

Gaillard, F., Reynaud, T., Thierry, V., Kolodziejczyk, N., & von Schuckmann, K. (2016). In situ based reanalysis of the global ocean temperature and salinity with ISAS: Variability of the heat content and steric height. *Journal of Climate*, *29*(4), 1305–1323. https://doi.org/10.1175/JCLI-D-15-0028.1

Gerkema, T., & Zimmerman, J. T. F. (2008). An introduction to internal waves: Lecture notes. Den Burg.: R. Neth. Inst. for Sea Res.

Gill, A. (1982). Atmosphere-ocean dynamics.

Grisouard, N., Staquet, C., & Gerkema, T. (2011). Generation of internal solitary waves in a pycnocline by an internal wave beam: A numerical study. *Journal of Fluid Mechanics*, *676*, 491–513. https://doi.org/10.1017/jfm.2011.61

Lévy, M., Franks, P. J. S., & Smith, K. S. (2018). The role of submesoscale currents in structuring marine ecosystems. *Nature Communications*, *9*(1), 4758. https://doi.org/10.1038/s41467-018-07059-3

Mahadevan, A. (2016). The impact of submesoscale physics on primary productivity of plankton. *Annual Review of Marine Science*, *8*, 161–84.

McWilliams, J. C. (2016). Submesoscale currents in the ocean. *Proceedings of the Royal Society of London A: Mathematical, Physical and Engineering Sciences*, *472*, 2189. https://doi.org/10.1098/rspa.2016.0117

Qiu, B., Chen, S., Klein, P., Wang, J., Torres, H., Fu, L.-L., & Menemenlis, D. (2018). Seasonality in transition scale from balanced to unbalanced motions in the World Ocean. *Journal of Physical Oceanography*, *48*(3), 591–605. https://doi.org/10.1175/JPO-D-17-0169.1

Renault, L., McWilliams, J. C., & Gula, J. (2018). Dampening of submesoscale currents by air-sea stress coupling in the Californian Upwelling System. *Scientific Reports*, *8*(1), 13388. https://doi.org/10.1038/s41598-018-31602-3

Rocha, C. B., Gille, S. T., Chereskin, T. K., & Menemenlis, D. (2016). Seasonality of submesoscale dynamics in the Kuroshio Extension. *Geophysical Research Letters*, *43*, 11,304–11,311. https://doi.org/10.1002/2016GL071349

Rodríguez, E., Wineteer, A., Perkovic-Martin, D., Gál, T., Stiles, B., Niamsuwan, N., & Rodriguez Monje, R. (2018). Estimating ocean vector winds and currents using a Ka-band pencil-beam doppler scatterometer. *Remote Sensing*, *10*, 576. https://doi.org/10.3390/rs10040576

Savage, A. C., Arbic, B. K., Alford, M. H., Ansong, J. K., Farrar, J. T., Menemenlis, D., et al. (2017). Spectral decomposition of internal gravity wave sea surface height in global models. *Journal of Geophysical Research: Oceans*, *122*, 7803–7821. https://doi.org/10.1002/2017JC013009

Shchepetkin, A. F., & McWilliams, J. C. (2005). The regional oceanic modeling system (ROMS): A split-explicit, free-surface, topography-following coordinate oceanic model. *Ocean Modelling*, *9*(4), 347–404. https://doi.org/10.1016/j.ocemod.2004.08.002

St. Laurent, L., & Merrifield, S. (2017). Measurements of near-surface turbulence and mixing from autonomous ocean gliders. *Oceanography*, *30*(2), 116–125. Retrieved from http://www.jstor.org/stable/26201858

Su, Z., Wang, J., Klein, P., Thompson, A. F., & Menemenlis, D. (2018). Ocean submesoscales as a key component of the global heat budget. *Nature Communications*, *9*(1), 775. https://doi.org/10.1038/s41467-018-02983-w

Torres, H. S., Klein, P., Menemenlis, D., Qiu, B., Su, Z., Wang, J., et al. (2018). Partitioning ocean motions into balanced motions and internal gravity waves: A modeling study in anticipation of future space missions. *Journal of Geophysical Research: Oceans*, *123*, 8084–8105. https://doi.org/10.1029/2018JC014438

Vic, C., Gula, J., Roullet, G., & Pradillon, F. (2018). Dispersion of deep-sea hydrothermal vent effluents and larvae by submesoscale and tidal currents. *Deep Sea Research Part I: Oceanographic Research Papers*, *133*, 1–18. https://doi.org/10.1016/j.dsr.2018.01.001

Vic, C., Naveira Garabato, A. C., Green, J. A. M., Spingys, C., Forryan, A., Zhao, Z., & Sharples, J. (2018). The lifecycle of semidiurnal internal tides over the northern Mid-Atlantic Ridge. *Journal of Physical Oceanography*, *48*(1), 61–80. https://doi.org/10.1175/JPO-D-17-0121.1

Wain, D. J., Lilly, J. M., Callaghan, A. H., Yashayaev, I., & Ward, B. (2015). A breaking internal wave in the surface ocean boundary layer. *Journal of Geophysical Research: Oceans*, *120*, 4151–4161. https://doi.org/10.1002/2014JC010416

Wunsch, C. (2015). *Modern observational physical oceanography*. Princeton, NJ: Princeton University Press.